CAAP Annual Report

Date of Report: November 10, 2016

Contract Number: DTPH5614HCAP03

Prepared for: Government Agency: DOT

Project Title: Experimental Characterization and Monitoring of Early Stage Corrosion Degradation of Pipeline Steels
Prepared by: Iowa State University

Contact Information: Professor Ashraf Bastawros,
T.A.Wilson Professor of Engineering
Department of Aerospace Engineering
2271 Howe Hall, Rm 1200
Ames, IA 50011-2271
Phone: 515-294-3039 Fax: 515-294-3262
Email: bastaw@iastate.edu

For quarterly period ending: September 30, 2016

Business and Activity Section

(a) Generated Commitments - None to report

(b) Executive Summary - The main objective of the proposed work is to enhance the pipeline safety through understanding the early corrosion mechanisms in high strength pipeline steels that lead to stress corrosion cracking with a focus on measurable degradation parameters that can guide the development of advanced NDE measurement procedures.

We have studied the electrochemical processes on high strength X70 pipeline steel exposed to high pH bicarbonate solution under laboratory conditions. The utilization of the nano-probes and in situ stress measurement during the electrochemical corrosion process have revealed many salient features for the early stage of SCC process. Within the experimental observation window, these findings, can be summarized as:

1. The detailed morphological and microstructure examination showed that the entire process is an acceleration of grain boundary grooving, accompanied with evolution of chemical product wedges around grain boundaries.
2. Electrochemical corrosion process starts aggressively, forming corrosion products (iron oxides). As the oxides thicken, iron transport is impeded, while the electrochemical ohmic resistance is increased. These combined processes greatly reduce the rate of the corrosion process.

3. The electrochemical corrosion-process is accompanied by an overall compressive residual stresses, which continue to amplify as the process progress. Such compressive residual stress are usually considered favorable as they may hinder the growth of further cracking. However, the nano- mechanical measurements probes showed that the volumetric expansion of the oxide resulted in tensile opening of the grain boundaries, while exposing the bulk of the surface grains to compressive stresses. Such wedging effect is one of the most significant mechanisms, driving the progression of SCC.
4. Within the laboratory observation time scale and conditions, the grain grooving extended to few microns in depth.
5. The electrochemical corrosion process has resulted in a soft layer near the surface with lower hardness (or flow stress). The nano-probe measurements showed about 20% drop in hardness, with no measureable changes in the elastic modulus. Our speculation is that the corrosion process has generated excessive atomic vacancies that is responsible for such drop.

(c) Corrosion Process Characterization

c.1 Experimental environment identification

This work focuses on high-pH intergranular stress-corrosion cracking (SCC) of high-strength low-alloy (HSLA) pipeline steel. Reports from the literature concur that SCC susceptibility is confined to a small window of electrochemical potential [1,2]. With respect to the current-potential curve, the susceptibility window extends from the potential at the maximum active dissolution current density of the polarization curve to the passivation potential. Armstrong [3] showed that both metal dissolution and corrosion product film formation occur at significant rates in this potential range. Potentiodynamic polarization curves on X70 pipeline steel samples in 1 M $NaHCO_3$ showed that the maximum active dissolution current density is at -0.60 V and the passivation potential at -0.40 V (all cited potentials are with respect to the Ag/AgCl reference electrode). On this basis, corrosion tests were carried out at three constant potentials within the SCC susceptibility window: -0.575 V, -0.521 V and -0.478 V. Concurrent electrochemical current and stress evolution were monitored at each potential. The current and stress transients were interpreted with the help of corrosion morphology characterization by SEM and profilometry.

The X70 pipe section was cut into 18 x 18 x 2 mm plates for testing in the electrochemical experimental setup, shown in Fig. 1. The working surface was ground with 600 and 1000 grit emery papers, followed by cleaning with deionized water and ethanol. All solutions were prepared from analytical grade chemicals and ultra-pure water (18.2MΩ-cm). Prior to the experiments, the working electrode was cathodically polarized at -0.978 V for 5 min to remove any oxides formed on the surface. Subsequently, open circuit potential was measured for 30 min, and the system was allowed to reach a stable corrosion potential. Potentiodynamic polarization or potentiostatic current measurements were then performed on the sample.

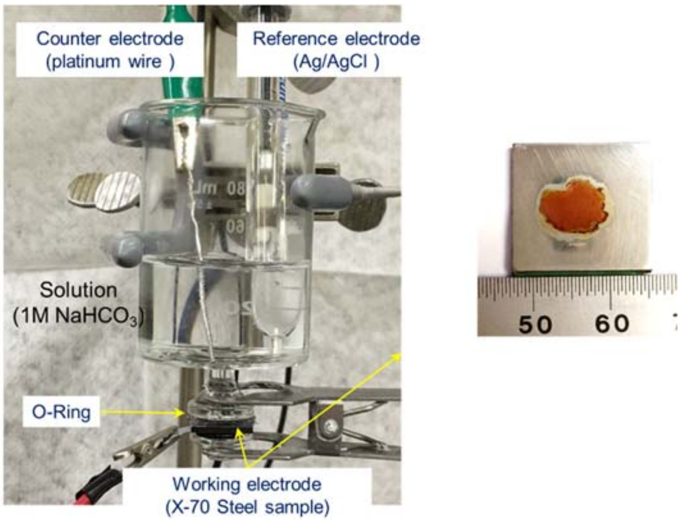

Figure 1: The utilized electrochemical cell showing the conventional three electrode, with steel samples as working electrode, platinum wire as counter electrode and Ag/AgCl reference electrode. Gamry Reference 3000 potentiostat was used as the power source. Dow Corning Vacuum Lubricant was applied between the sample and the O-ring to eliminate crevice corrosion.

c.2 Corrosion induced stresses in the near surface layers

Phase-shifting curvature interferometry was used to monitor the stress transients during the three different corrosion conditions [4,5]. Corrosion induced stresses in the sample was determined from the curvature changes in the steel specimen using Stoney's equation for substrate curvature [6].

$$F = \left(\langle \sigma_{react} \rangle \right) h_{react} = \frac{E_s h_s^2}{6(1-\nu)} \Delta k$$

Where F is the in-plane force per unit width in the film, E_s Young's modulus of the substrate, h_s is the substrate thickness, ν is the Poisson's ratio, and k is substrate curvature. The enhanced curvature resolution of the utilized setup (shown in Fig. 2) permits stress measurements in relatively thick sheet and foil samples, in contrast to thin metal films typically used for deflection techniques.

Specimens of X70 steels with dimensions of 30 mm length X 12 mm width and 0.7 mm thickness were cut from a pipeline specimen. The front surface of the sample was ground using1000 grit sandpaper to remove machining grooves and to obtain a uniform surface roughness. The back surface of the specimens was mirror-polished to enable curvature measurements. The specimens were mounted in the electrochemical cells shown schematically in Figure 1 such that front surface is exposed to corrosion while the back surface is utilized for monitoring the stress development using phase-shifting curvature interferometry.

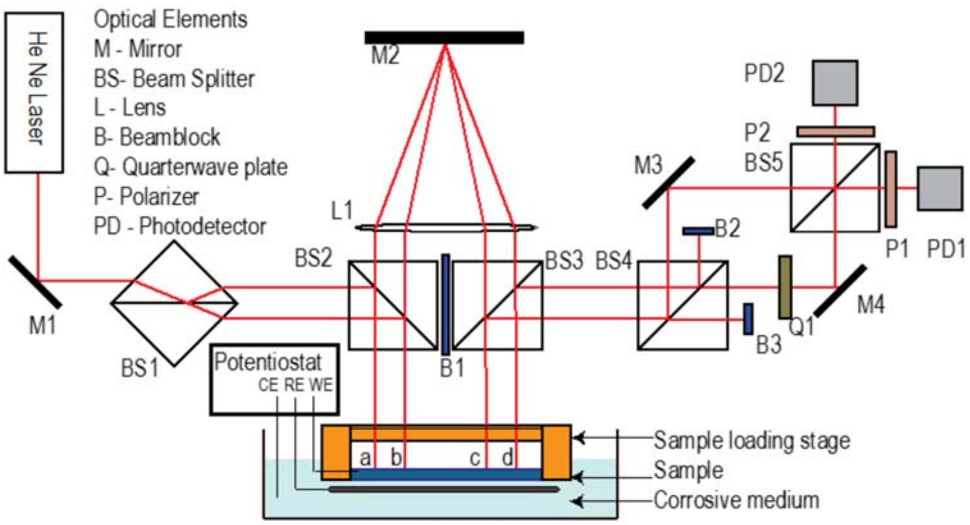

Figure 2: Schematic of the setup of interferometry system, which also shows the setup of the samples.

Prior to each constant potential corrosion experiment, the steel samples were held at a potential of -0.978 V to cathodically reduce the native oxide layer. Figure 3(a) shows the typical current and stress transients obtained after stepping the potential to the test potential for all three potentials. Fig. 3 (b) shows the decaying portion of the current transients during the first several seconds. Similar current decays reported in the literature are associated with the formation of a passive or pre-passive oxide-carbonate layer on the initially unfilmed steel surface [3]. Microscopic examination after the initial current decays revealed no evidence of preferential grain boundary corrosion.

The current density increased after the initial decays. SEM observations at -0.521 V showed that the current rise to the maximum at 17 mins was accompanied by visible grain boundary corrosion as shown on Fig. 4. Profilometry indicated that corrosion product accumulated on the steel surface during the subsequent current decay as shown on Fig. 12. It seems likely that the current rise after the minimum was caused by intergranular corrosion increasing the actively corroding steel surface area. Dissolved iron ions produced by intergranular corrosion eventually produced a precipitated iron hydroxy-carbonate corrosion product on the outside surface. The increasing diffusion resistance of the growing precipitate layer likely explains the current decay [7]. The current transient at -0.478 V was qualitatively similar to that at -0.521 V, but the smaller times of the current minimum and maximum suggested that grain boundary attack and precipitation occurred at smaller times, as a result of the higher electrochemical driving force for iron oxidation at the more positive potential. At -0.575 V, no current maximum was observed, implying that no precipitated corrosion product was present.

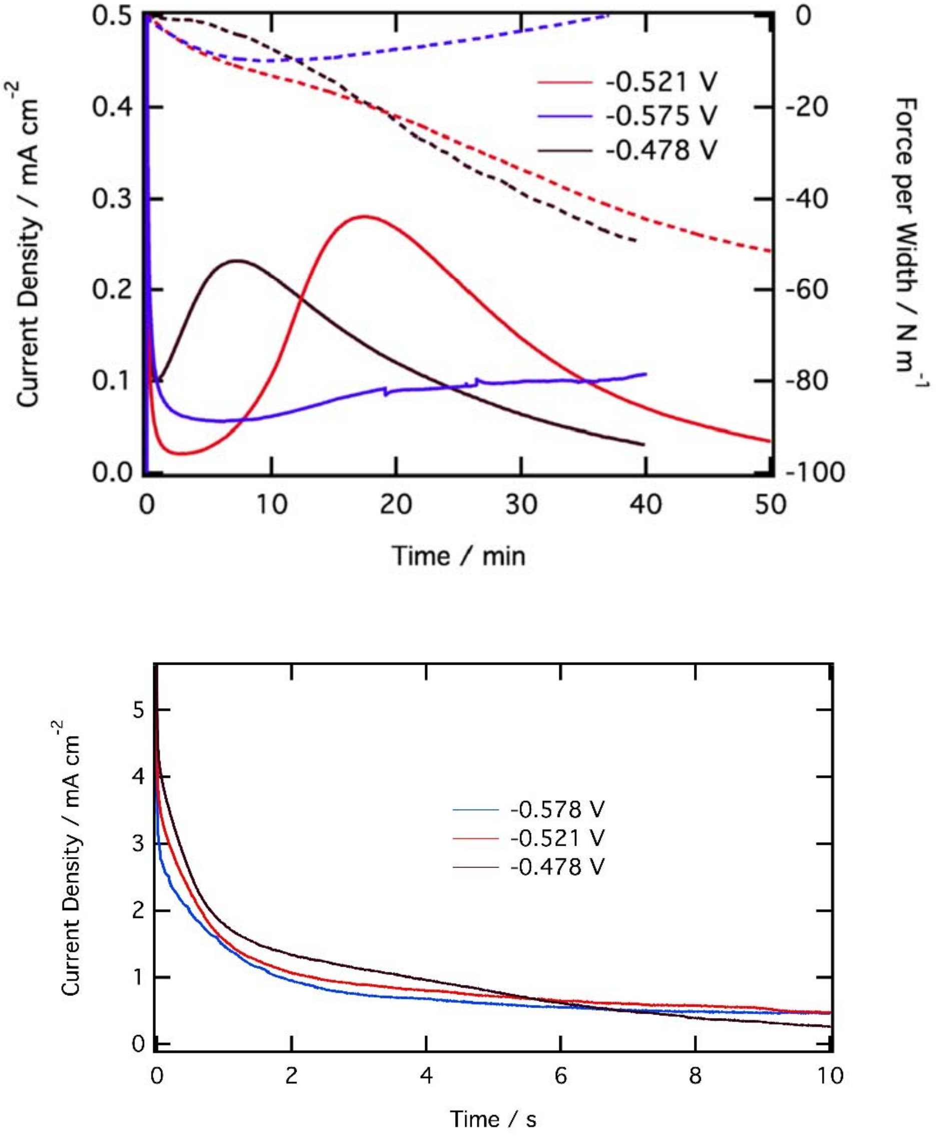

Figure 3: Typical stress and current transients measured during corrosion exposure at three different potentials in the SCC susceptibility region. (a) Atypical current and stress transients obtained after stepping the potential to the test potential for all three potentials. (b) The decaying portion of the current transients during the first several seconds

Stress transients measured at -0.478 V and -0.521 V show similar dependence on the current transients with monotonic development of compressive stress during the 2 hours of sample exposure. However, at -0.575 V, measured stress transients are very different with non-monotonic stress development during the corrosion experiments. During the initial current decay immediately after exposure, compressive stresses rapidly develop in the sample at all three corrosion potentials. At -0.478 V and -0.521 V, compressive stress development becomes slower after the initial decay as the current magnitude increases. After the current reaches the peak value and starts decaying, compressive stresses start building in the sample at a faster rate. Final value of compressive stresses after 2 hours of exposure in both conditions is similar in magnitude. At -0.575 V, the stress development during the initial current decay is compressive but after that period as the current reaches a constant value, tensile stresses develop in the sample. After 2 hours of exposure at -0.575 V, the sample surface is loaded in tension.

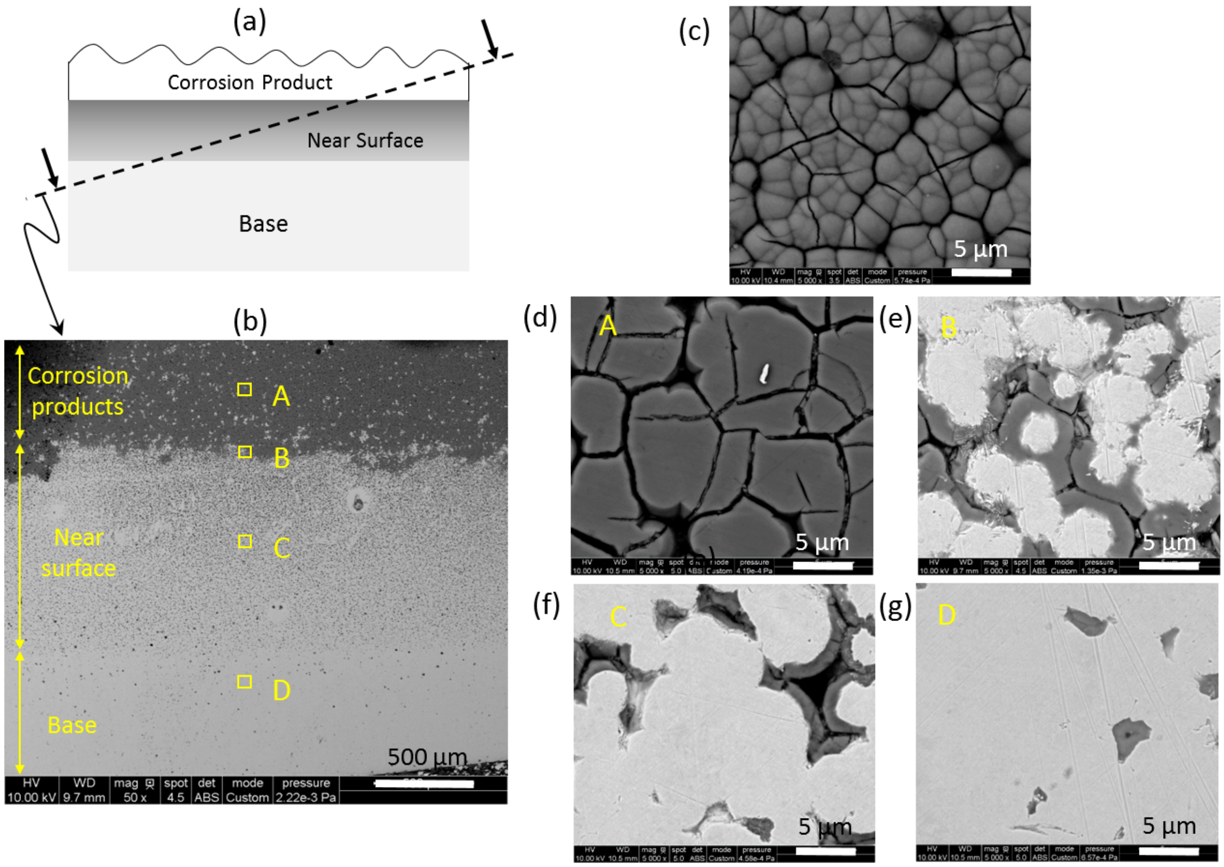

Figure 4: SEM surface analysis of the corrosion experiment at -0.521V. (a) A sketch of the observed near-surface damage evolution as a result of a typical corrosion experiments, and the shallow angle polishing plane. (b) SEM image of the inclined polishing plane, showing locations of high resolution (c-g) SEM images for the progression of the corrosion process into the surface.

Measured stress transients are also plotted as function of corrosion density for the three different conditions in Fig.5. The charge density was computed by integrating the current density from the start of the corrosion exposure to the time corresponding to each stress measurement. The plots clearly show the stress development during exposure at both -0.478 V and -0.525 V follows a similar dependence with initial rapid stress development during the current decay, subsequent period of slow increase during the current buildup to peak and rapid increase after the current reaches a peak value. In the case of -0.478 V, the decay and buildup to peak current value happens in a shorter duration after exposure to corrosion potential as compared to -0.521 V. It is interesting to note after the peak current, the slope of stress vs charge density is similar at both -0.478 and -0.521 V. These results show that at conditions within the SCC susceptibility region (-0.478 V and -0.521 V), compressive stresses develop in the sample indicating that the in-plane dimensions of the near surface layers has increased due to the corrosion exposure. While at the boundary of the SCC susceptible regions (-0.575 V), tensile surface develop in the sample after prolonged exposure indicating that in-plane dimensions of the near surface layers have decreased during the corrosion exposure.

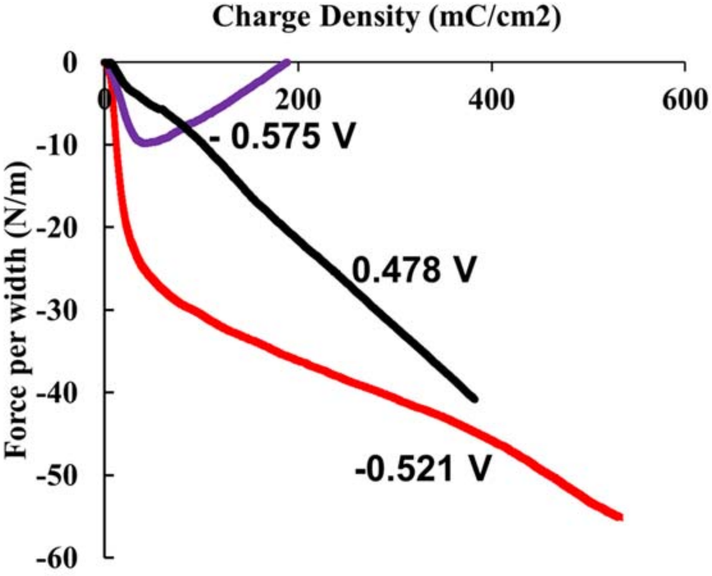

Figure 5: Measured stress transient plotted as function of corrosion charge density at three different potentials in the SCC susceptibility region.

Studies of intergranular corrosion morphology were carried out at each of the three test potentials after ~2 hr corrosion exposures. Cross-sections revealing the intergranular corrosion morphology were prepared by shallow-angle polishing (cf Fig.4 for -0.521V). SEM examination indicated extensive subsurface attack of all three samples. At -0.575 V, the cross-sections revealed significant dissolution of internal grains along intergranular corrosion pathways. On the other hand, almost no subsurface solid corrosion product was detected, except very close to the external surface.

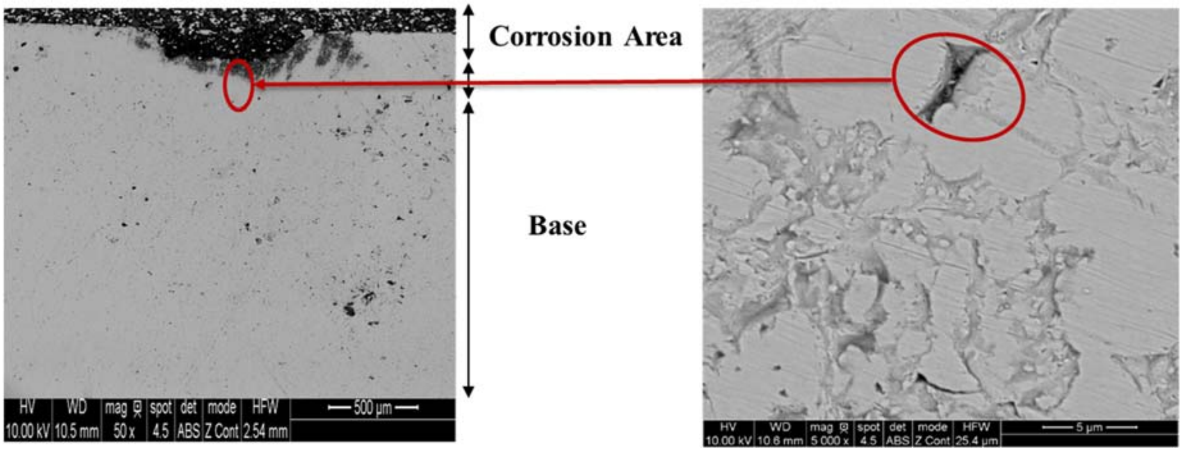

Figure 6: SEM surface analysis of the corrosion experiment at -0.575V. The cross-sections revealed significant dissolution of internal grains along intergranular corrosion pathways.

There was little evidence of an external precipitated layer, consistent with the absence of a current maximum at this potential. In contrast, the cross-sections of samples tested at the two highest potentials exhibited extensive internal and external corrosion product formation. The internal corrosion product was produced by steel oxidation along grain boundaries. The external product consisted of a particulate layer coating the outside surface of the steel. EDS indicated that the main constituents of both corrosion products were iron, oxygen and carbon in similar proportions, suggesting that both products were iron hydroxy-carbonate compounds as shown in Fig. 7 & 8. Similar film compositions are found in other studies of steel corrosion in carbonate media [4]. Nanoindentation tests described in detail below revealed that the elastic modulus and hardness of the internal corrosion product were significantly greater than those of the external product. Thus, the internal product is a dense, compact hydroxy-carbonate layer coating the corroded grain boundary surfaces, while the external product is a porous granular precipitate. The electrical and diffusion resistances of the internal grain boundary film likely significantly exceed that of the precipitated layer.

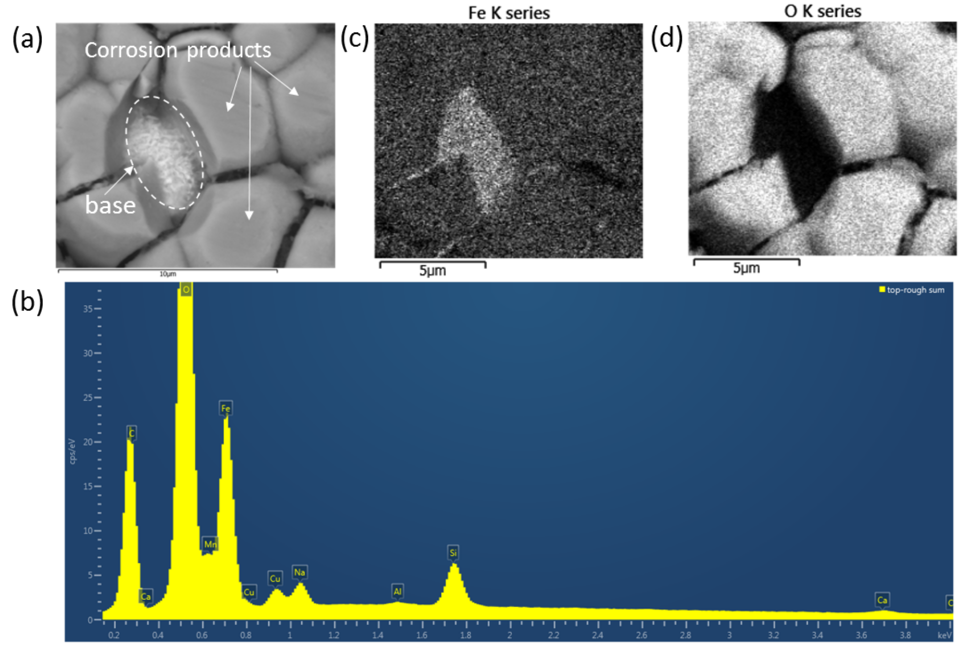

Figure 7: (a) SEM image of the top surface within the corrosion product, and the base material underneath, (b) Energy-dispersive X-ray spectroscopy (EDS) spectrum showing the dominant elements, and EDS maps for (c) Iron (Fe), (d) Oxygen (O).

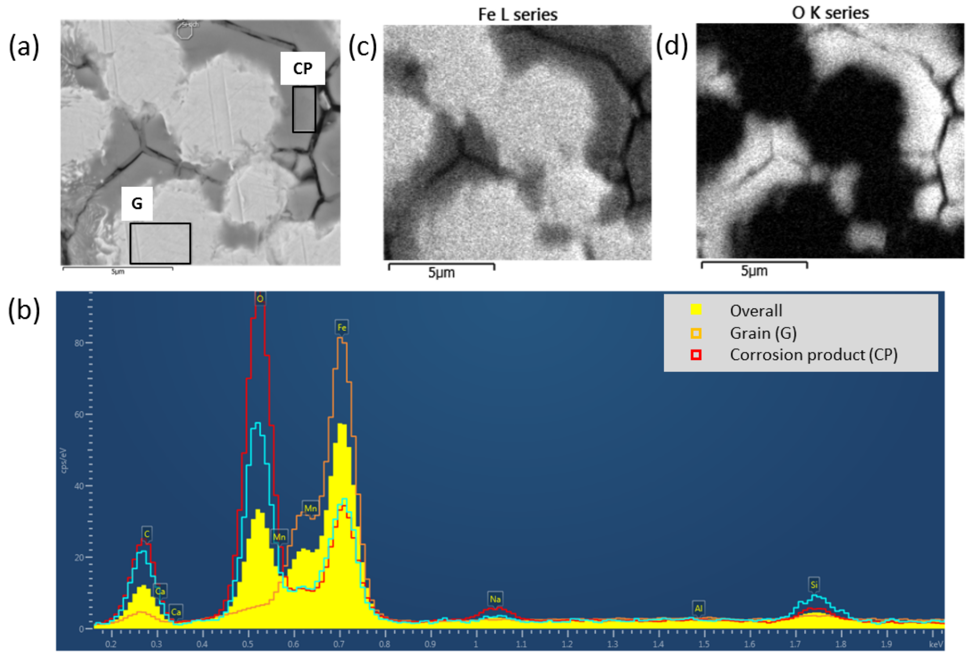

Figure 8: (a) SEM image of the region on the interface between corrosion product particles and the grains (marked as B in Fig. 1(b)). (b) EDS spectrum showing the dominant elements for different region on the (a), (c) EDS map for Iron (Fe), and (d) EDS map for Oxygen (O).

In the cross section samples, the intergranular corrosion morphology deep within the corroded layer results from newly initiated corrosion, while that close to the outer surface reflects a later stage of grain boundary corrosion development. Hence, the time evolution of corrosion at a given depth can be inferred by comparing images of grain boundaries at different depths. Such an analysis is depicted on Fig. 9, and reveals the following stages of development of intergranular attack at a given depth: (i) Upon first contact with solution, corrosion on both sides of the grain boundary generates a corrosion product film which fills the entire grain boundary crevice. (ii) With continued grain boundary corrosion, the film grows in thickness and simultaneously the metal grain decreases in size. Steady consumption of metal apparent in the images suggests that the iron ions can be transported through the compact corrosion product film. (iii) The corrosion product film reaches a steady-state thickness while the diameter of the metal grains continues to decrease. Accordingly, the grain boundary crevice widens and the steel becomes increasingly porous. Stage (iii) corresponds to a steady-state passive film, through which metal ions migrate at a constant rate before dissolving at the film-solution interface [8]. Comparison of images at the two higher potentials shows that a given depth, the ratio of corrosion product to steel volume at -0.478 V is greater than that at -0.521 V. On the other hand, a similar corrosion morphology is evident close to the surface at -0.521 V as that at the midpoint the IGC layer at -0.478 V. Thus, it seems that at -0.478 V the progression through Stages (i) - (iii) occurs more rapidly than at -0.521 V. As discussed above, a parallel conclusion is suggested by the current transients.

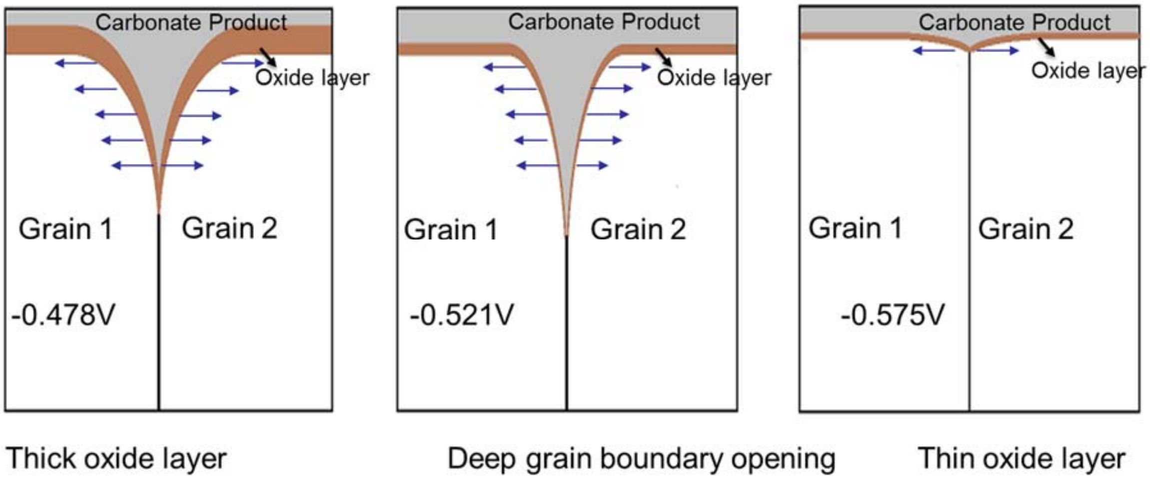

Figure 9: Stages of development of intergranular attacks at different potentials.

c.3 Utilization of Nanoindentation to Understand the IGSCC Mechanism

c.3.1 Characterization of Top Corrosion Product Layer by Nanoindentation:

The mechanical properties of the corrosion product deposited on the sample surface were measured by high load quasi-static indentations. Hysitron TI 950 TriboIndenter with the high load transducer (load range of 0-500mN) was utilized under force control mode. A trapezoidal loading profile, which consists of a 5s linear loading, 2s hold at the peak load, and 5s linear unload, was applied to impose the regular patterns of indents using a Berkovich indenter tip. A sequence of indentations were performed on each sample with progressive increase of the peak load between 1mN to 250mN. Such loading range resulted in a maximum indentation depth of 4 μm.

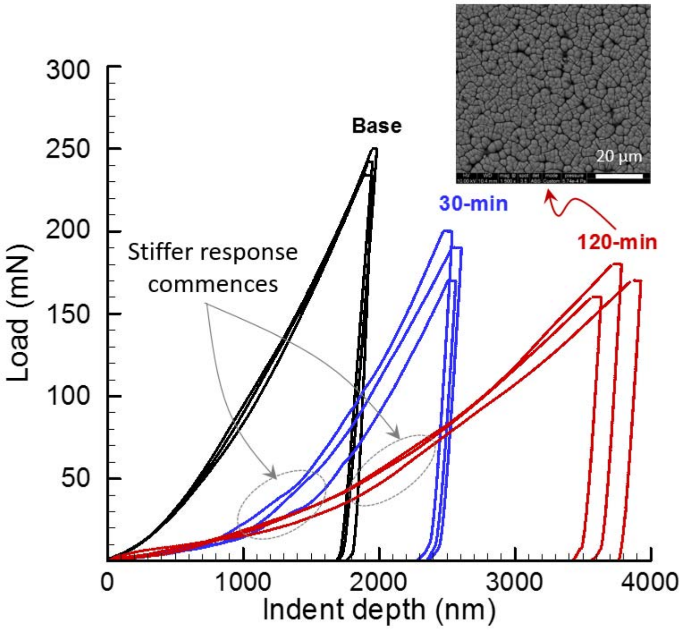

Figure 10: A representative set of force-indentation depth curves for the base (no corrosion), 30 min and 120 min corroded samples. The insert is an SEM image of the surface of 120 min corroded sample, showing the product layer precipitated on the sample surface.

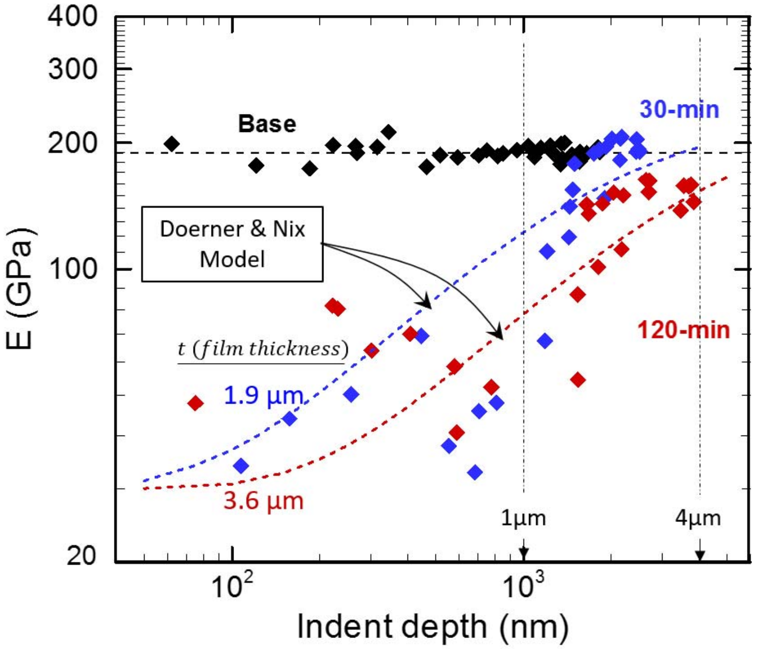

Figure 11: Indentation modulus as a function of indentation depth for the corrosion product layer for 30 min and 120 min corroded samples, showing the extent of the corrosion products. The products layer has a modulus of about 30% the base steel. The dashed lines show the corresponding modulus profiles projected by Doerner & Nix [10] model for 1.9µm and 3.6 µm thick product layers.

Figure 10 depicts a representative set of force- indentation depth curves for the base (no corrosion), 30 min and 120 min corroded samples. For the corroded samples, one can clearly note a transition from softer to stiffer material response at a characteristic indentation depth of about 1μm for 30 min exposure time, and 2μm for 120 min exposure time. Such change in the loading stiffness can be attributed to a transition from the soft corrosion product layer to bulk base material.

Figure 11 shows the variation of the indentation modulus E (derived from the contact analysis by Oliver and Pharr [9]) as a function of the indent depth for the examined three cases. For the base sample, E is around 190GPa, and is independent of the indentation depth. Though, a noticeable drop on E can be seen for the corroded samples with chemical products. The corrosion product layer has a modulus of about 25% that of the base material (E~60GPa) with a depth of ~1200nm for 30 min exposure and ~2000nm or more for the 120 min exposure. It should also be noted that the measurements were carried out in the dry state. It remains to be seen if the hydroxylated state might exhibit the same stiffness, as such layer may contribute to the balance of the residual stresses developed during the corrosion process.

In order to estimate the thickness of the product layer, we utilized an empirical model proposed by Doerner and Nix [10], which was originally suggested to consider the influence of the substrate on the measured indentation modulus for thin film-substrate systems. Accordingly, the measured indentation modulus can be expressed as follows;

$$\frac{1}{E}=\frac{1}{E_f}+\left(\frac{1}{E_s}-\frac{1}{E_f}\right)\exp\left(\alpha\frac{t}{a}\right)$$

where E_f is film modulus $\left(E_f \approx 30GPa\right)$, E_s is the substrate modulus $\left(E_s \approx 200GPa\right)$, t film thickness, a is the indenter contact radius, and α is the material dependent fitting parameter $\left(\alpha = 0.17\right)$. Accordingly, the thickness of the product layer was estimated around 1.9μm for 30 min corroded sample, and 3.6 μm for 120 min corroded sample by least square fitting of the experimentally measured modulus data. In Figure 3, the dashed lines show the corresponding modulus profiles projected by Doerner & Nix model. Such thickness estimations are in very good agreement with the thickness measurements performed by 3-D optical surface profiler Zygo NewView™ 5200 shown in Fig. 12. The average thickness of the corrosion products precipitated on the sample surface is measured as ~2 μm after 30 min exposure, and ~4 μm after 120 min exposure times.

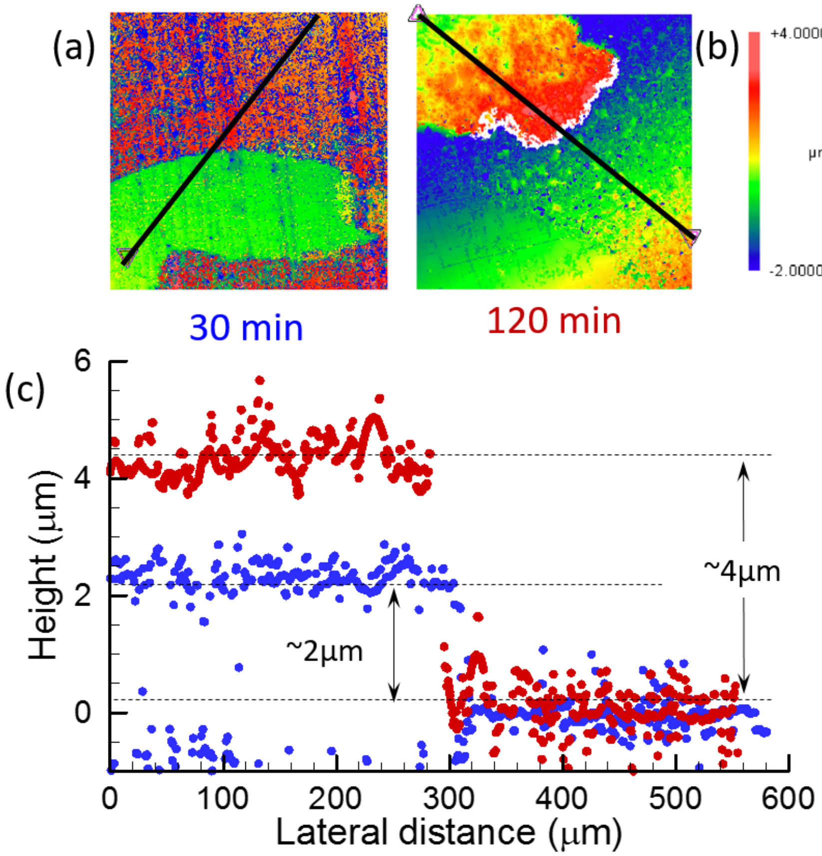

Figure 12: (a, b) Surface profiles for 30 min and 120 min corroded samples, captured by 3-D optical surface profiler Zygo NewView™ 5200, (c) the corresponding height profiles along the lines shown in (a, b).

c.3.2 Characterization of Near-surface Material Evolution and IGSCC Mechanism by Nanoindentation:

Then preferential anodic dissolution commences at GBs, accelerating the grain boundary grooving with evolution of chemical product wedges around GBs. Such extensive intergranular corrosion activity might suggest a degradation of the material properties in the vicinity of the GBs. In order to probe a possible changes of mechanical properties in the vicinity of the GBs, we have performed sets of quasi-static shallow indentations on the angle polished surface of 2 hour corroded sample (at -0.521 V) as shown in Figs. 13(a, b). Nanoindentations were placed on a line traversing the GB using Hysitron TI 950 TriboIndenter with 90° cube corner indenter tip under force control mode. The nanoindents were introduced on the surface under a constant load of 250 µN, with inter-indentation spacing of 500 nm. Figure 13(c) shows an atomic force microscope (AFM) image in surface topography mode rendering the GB and the imposed lines of the nanoimprints. This range of loading would limit the indentation to the initial sink-in range [11, 12] as well as limiting the indentation process zone to about 150nm. The corresponding indentation Hardness, H, and Modulus, E, were extracted from indentation force-displacement curves using Oliver-Pharr method [9].

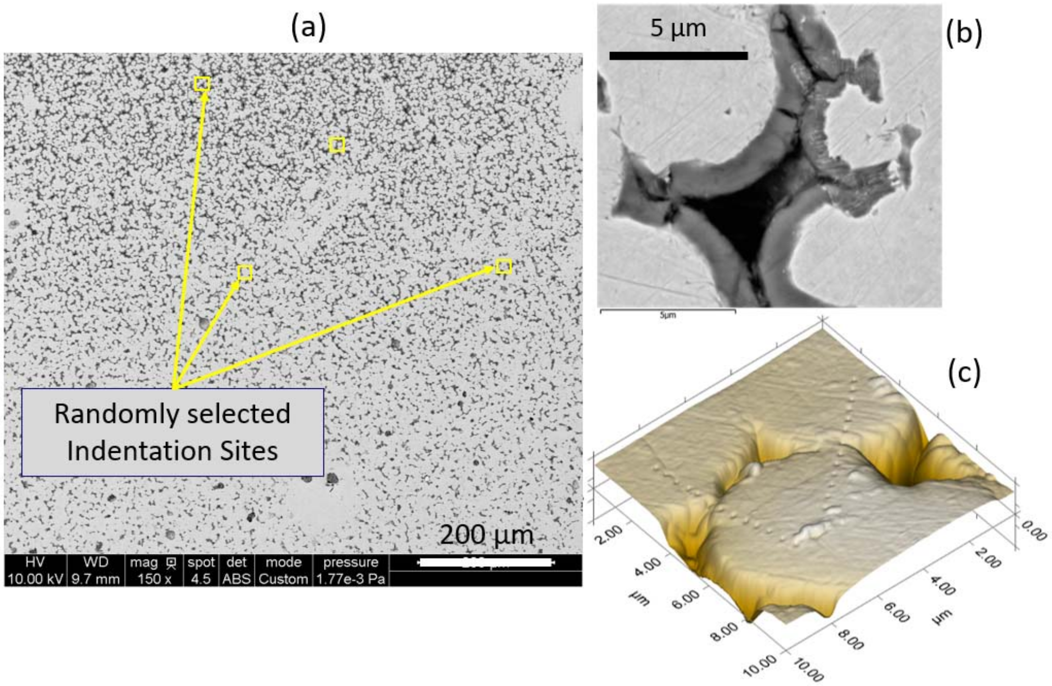

Figure 13: (a) A scanning electron microscope (SEM) image of the angle polished surface of the 120 min corroded sample at -0.521 V showing the near surface region, (b) close-up SEM image of the near surface region showing the GB grooving and formation of corrosion products at the GBs, (c) an atomic force microscope (AFM) image in surface topography mode rendering the GB and the imposed lines of the nanoimprints.

We have observed two distinct behaviors among all sets of line indentations traversing different GBs. The first was identified on an indentation site as shown in Fig. 14(a), which shows the imposed line of the nanoimprints. The variations of H and E as a function of lateral distance measured from the GB-line are shown in Fig. 14(b, c), respectively. The measured H exhibits about 20-30% drop across the GB from that measured in the middle of the grains, whereas the measured E ranges within 10% of the base value. The presented trend is atypical on many other sets of GB near a GB corrosion wedge. The observed trend from the nanoindentation measurement suggests the existence of a softened layer of the order of 1 μm in the vicinity of the GB as a result of the corrosion process. Such observed softening might arise from the anodic dissolution of iron ions, leaving behind clusters of secondary defects (atomic vacancies) that might lead to such drop in local hardness.

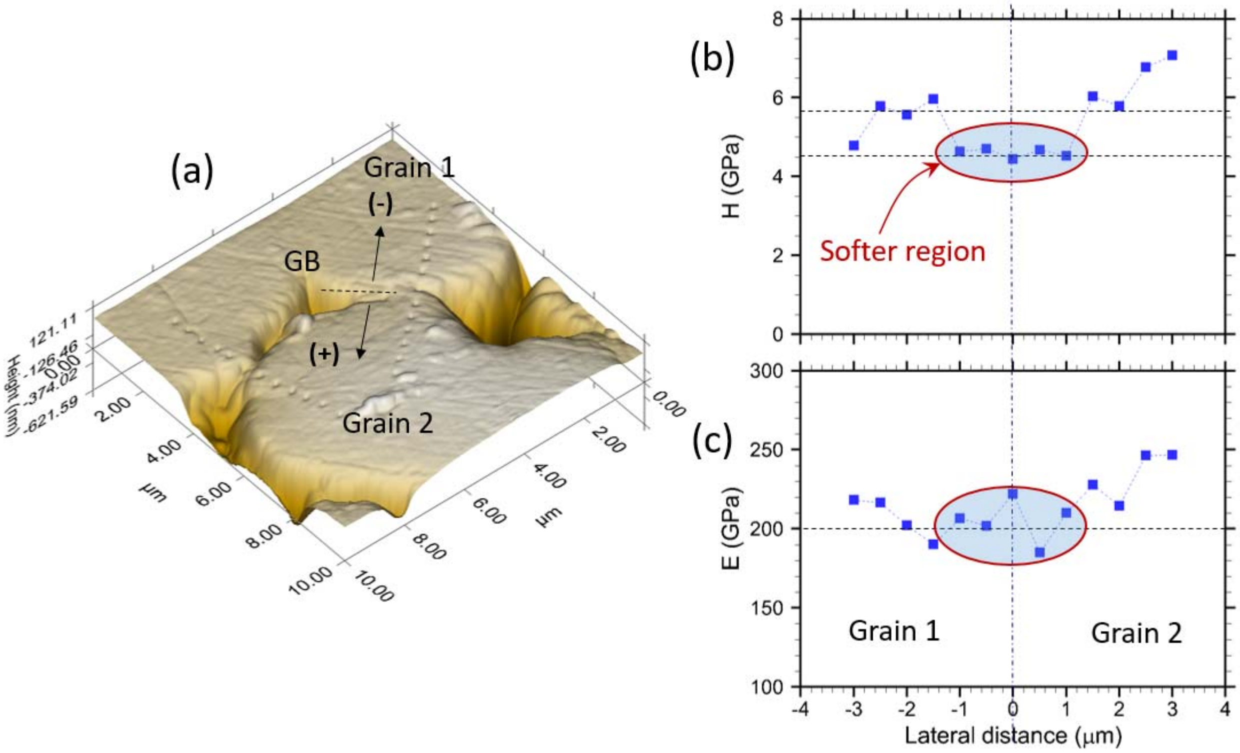

Figure 14: (a) An atomic force microscope (AFM) image in surface topography mode rendering the GB and the imposed lines of the nanoimprints, (b, c) The variations of H and E as a function of lateral distance measured from the GB-line, showing the existence of a softened layer of the order of 1 μm in the vicinity of the GB as a result of extensive intergranular corrosion process.

On top of the observed GB softening behavior, we have also identified formation of the corrosion product at the GB as shown in Figure 15(a) showing the imposed line of the nanoimprints. On this lines, both H and E exhibited large drop, and reached those of the corrosion product layer (independently measured on the surface film as $E \approx 25GPa, H \approx 1.6GPa$). While the oxide layer is less than 1 μm thick, the reduced values extend to a depth of about 2 μm from each side of the GB. In addition to that, one can note that H tends to increase from the corrosion product level to the average grain level as it approaches to the center of the grain-2, whereas there is no noticeable change recorded in E. Such nanoindentation measurements supports the predicted near-surface microstructural evolution observed by SEM imaging as shown in Fig. 15(a). To further elucidate the observed mechanism, another set of line nanoindentations traversing the GB at the cross-section of one the GB grooves as shown in Fig. 15(b). Figure 15(c) is an AFM image of the surface topography rendering of the triple junction and GBs and the imposed lines of the nanoimprints.

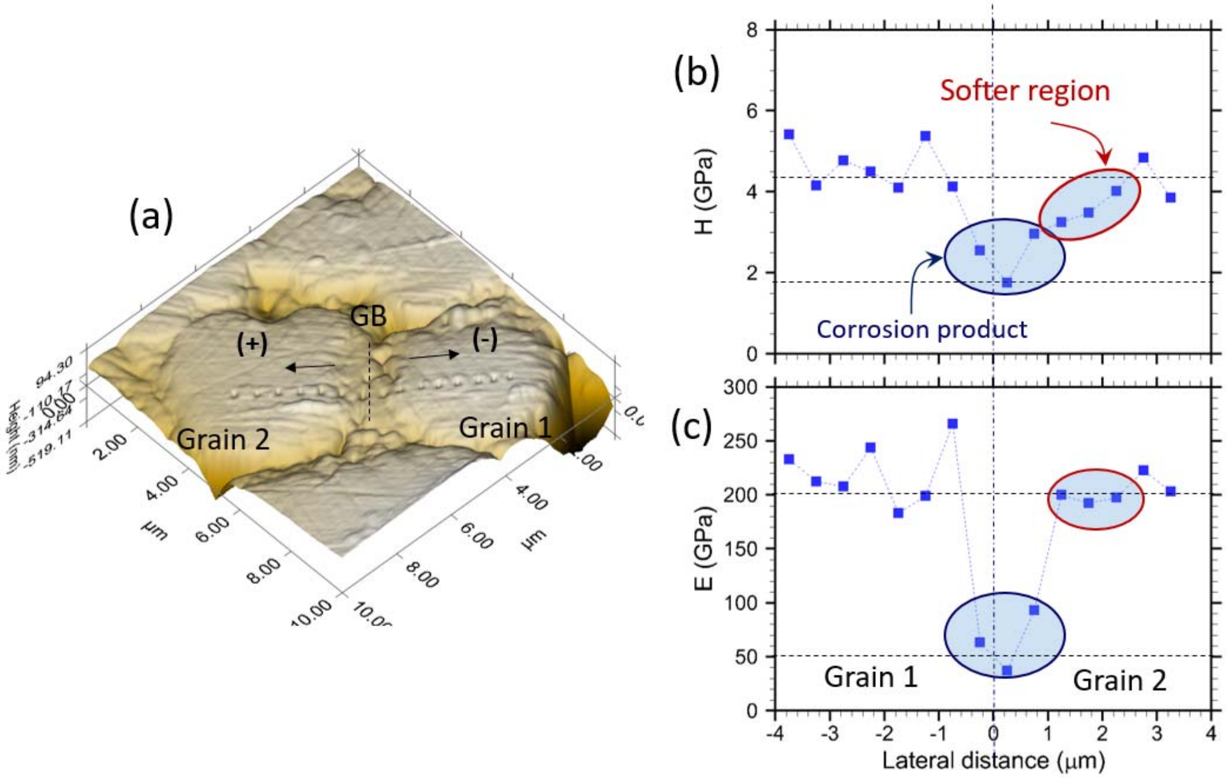

Figure 15: (a) An atomic force microscope (AFM) image in surface topography mode rendering the GB and the imposed lines of the nanoimprints, (b, c) The variations of H and E as a function of lateral distance measured from the GB-line, showing the existence of both the 1-2 µm thick corrosion product layer formed at the GB and a softened layer of the order of 1 µm in the vicinity of the GB as a result of extensive intergranular corrosion process.

The variations of H and E as a function of lateral distance measured from the GB-line are shown in Fig 16(a, b), respectively. We can identify both the dense corrosion product deposited at the GB walls, and the softened region within grain-1 near the GB. Figure 16(c) shows a representative set of force- indentation depth curves obtained at the center of the grain-2 (black lines) and in the region near to the GB (blue and red lines). One can easily identify displacement burst events, which are generally associated with homogenous dislocation nucleation/propagation. In addition, it is generally assumed that the first dislocation burst occurs when the maximum shear stress under the indenter tip is of order of the theoretical shear strength of the material (Peierls-Nabarro stress). The critical load for the first displacement bust can be associated with theoretical strength of the material through the following expression,

$$\tau_{PN} \approx \tau_{\max} = 0.31\left(\frac{6E^2}{\pi^3 R^2}P_{cr}\right)^{1/3}.$$

It should be noted that the critical load in the near GB region is lower than that measured at the center of the grain by ~30-40%. Accordingly, we can argue that the theoretical shear strength of the material is decreased by 10-15% within the observed softer region near the GBs. In addition, the total length of the displacement bursts is relatively higher in these regions compared to the that measured at the center of the grains. Such increase can be related to enhanced atomic vacancy density as a result of intergranular corrosion activity.

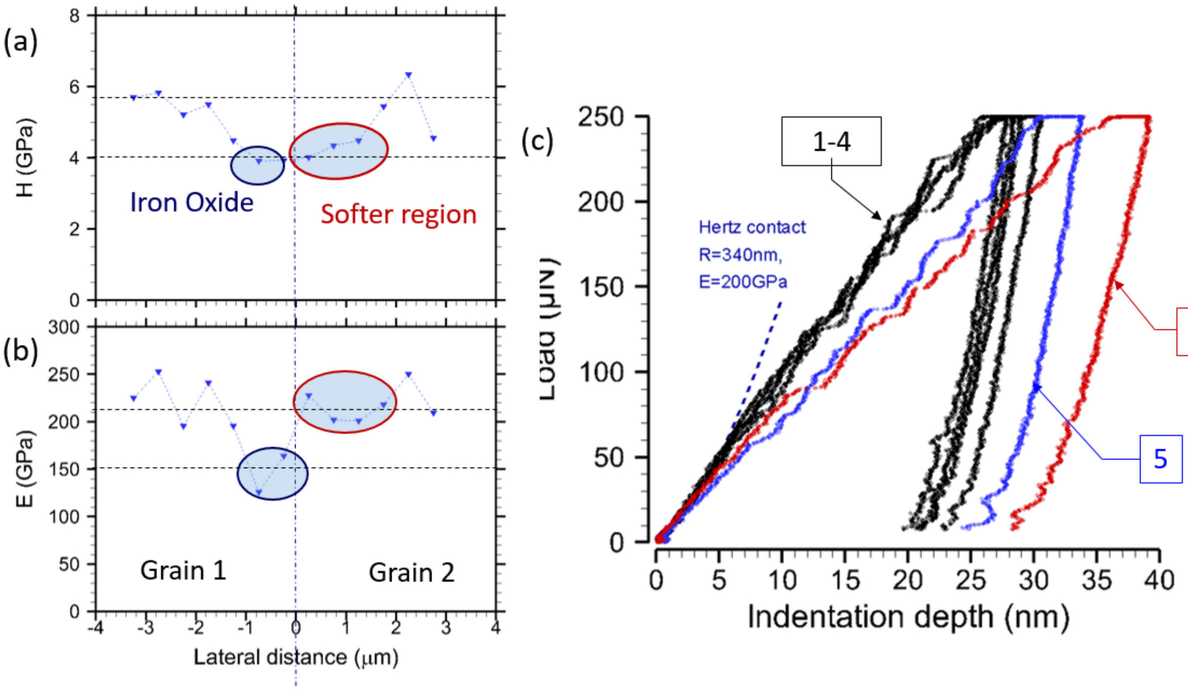

Figure 16: (a, b) The variations of H and E as a function of lateral distance measured from the GB-line (as shown in Fig. 17(c)), (c) a representative set of force- indentation depth curves obtained at the center of the grain-2 (black lines) and in the region near to the GB (blue and red lines).

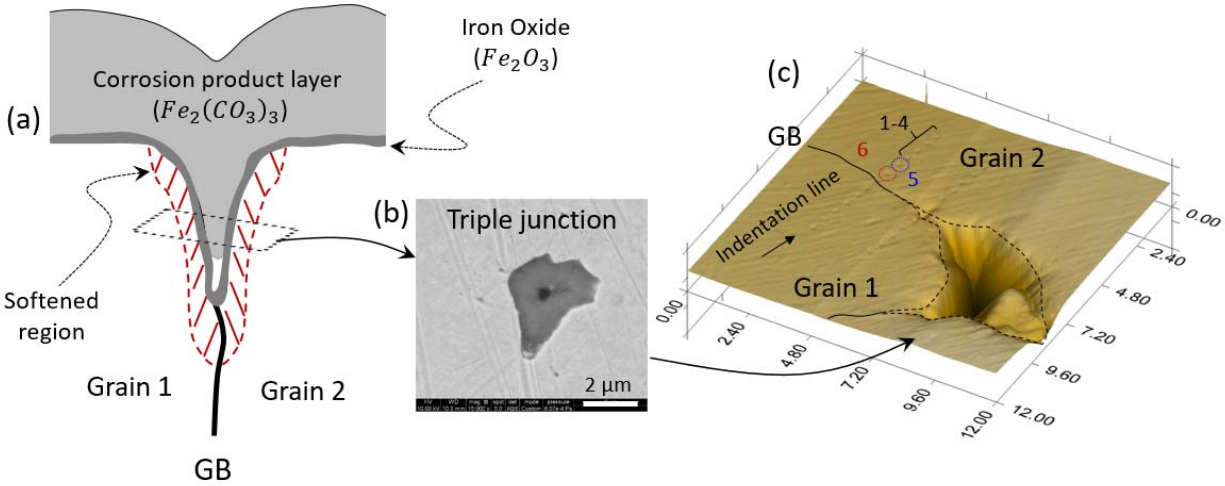

Figure 17: (a) The proposed near-surface microstructural evolution as a result of intergranular corrosion activity, (b) A scanning electron microscope (SEM) image of the cross-section of the GB grooves showing the triple junction, (c) an atomic force microscope (AFM) image in surface topography mode rendering the triple junction and GB and the imposed lines of the nanoimprints.

c.4 Summary

In summary, the electrochemical experiments and studies of morphology development reveal that extensive intergranular corrosion occurs at potentials of maximum SCC susceptibility. In this potential range, a high fraction of the grain boundaries is attacked as depicted on Fig. 17. At a given depth, grain boundary corrosion follows a characteristic progression beginning with formation of iron hydroxy-carbonate corrosion product filling the grain boundary crevice. Continuing metal dissolution causes the crevice to widen while the product film reaches a steady-state thickness. At the leading edge of the grain boundary crevice, localized compressive wedging stresses may result from corrosion product filling the entire crevice. Such stresses may play a direct role in IGC penetration and, in the presence of external stress, may assist stress corrosion crack initiation. Similar wedging stress mechanisms for SCC have been proposed in other systems [4]. The role of grain boundary corrosion product formation in intergranular SCC would explain why SCC occurs only at potentials where both metal dissolution and oxidation simultaneously occur. The stress measurements reported below will further elaborate stress generation mechanisms during intergranular corrosion.

(d) References Cited

1. R. D. Armstrong, A. C. Coates, A Correlation Between Electrochemical Parameters and Stress Corrosion Cracking, Corrosion Sci., 16 (1976) 423-433.
2. R. N. Parkins and S. Zhou, The Stress Corrosion Cracking of C-Mn Steel in CO_2-HCO_3^--CO_3^{2-} Solutions. II. Electrochemical and Other Data, Corros. Sci., 39 (1997) 175-191.
3. A. M. Riley, J. M. Sykes, Active-Passive Transition in Low Alloy Steels in Carbonate Solutions, Electrochim. Acta, 35 (1990) 35-45.4.
4. Wang J., Shrotriya P., Kim K.S., Surface residual stress measurement using curvature interferometry, Exp Mech, 46, 39-46 (2006).
5. Capraz O.O., Hebert K.R., Shrotriya P., In Situ Stress Measurement During Aluminum Anodizing Using Phase-Shifting Curvature Interferometry, J. Electrochem. Soc. 160, D501 D506 (2013).
6. Stoney, G.G., The tension of metallic films deposited by electrolysis. Proceedings of the Royal Society of London. Series A, Containing Papers of a Mathematical and Physical Character, 1909. 82(553): p. 172-175.
7. B. Ingham, M. Ko, N. Laycock, N. M. Kirby, D. E. Williams, First stages of siderite crystallisation during CO_2 corrosion of steel evaluated using *in situ* synchotron small- and wide-angle X-ray scattering, Faraday Discuss. 180 (2015) 171-190.
8. R. Kirchheim, Growth Kinetics of Passive Films, Electrochim. Acta, 32 (1987) 1619-1629.
9. Oliver W.C., Pharr G.M. An Improved Technique for Determining Hardness and Elastic Modulus using Load and Displacement Sensing Indentation Experiments. Jounal of Material Research, **7**, 1564-1583 (1992).

10. Doerner, M. F., & Nix, W. D. A method for interpreting the data from depth-sensing indentation instruments. Journal of Materials research, 1(04), 601-609, (1986).
11. Yang, C., Lo, C.T., Narasimhan, B., and Bastawros, A.-F., Measurements of Diffusion Thickness at Polymer Interfaces by Nanoindentation: A Numerically Calibrated Experimental Approach, Journal of Materials Research, 24(3), 970-977, (2009).
12. Taljat B., Zacharia T., Pharr G.M., Pile-up behavior of spherical indentations in engineering materials, in Fundamentals of Nanoindentation and Nanotribology, edited by Moody N.R., Gerberich W.W., Burnham N., and Baker S.P. (Mater. Res. Soc. Symp. Proc. 522, Warrendale, PA, 1998), p. 33.